

Cite this: *Mater. Adv.*, 2022,
3, 6373

Fabrication of a recyclable magnetic halloysite-based cobalt nanocatalyst for the efficient degradation of bisphenol A and malachite green†

Bhavya Arora,  Shivani Sharma, Sriparna Dutta, Sneha Yadav, Pooja Rana, Priyanka and R. K. Sharma *

Worsening water quality has drawn considerable attention from the scientific fraternity owing to its serious impact on human health and environmental ecosystem. In this regard, magnetic halloysite-based organic–inorganic hybrid materials with a hollow nanotubular structure and surface tunable chemistry have emerged as an excellent platform for the efficient removal of recalcitrant water contaminants. The fabrication of nanocatalyst involves a simple yet versatile covalent immobilization strategy, wherein a chelating ligand, 2-benzoylpyridine (2-BPy) was grafted onto silane-functionalized magnetic halloysite nanotubes with subsequent anchoring of cobalt ions. Various physico-chemical techniques such as FT-IR spectroscopy, P-XRD, VSM, FE-SEM, TEM and XPS provided valuable insights into the crystallinity, magnetic attributes and morphology of the designed nanocomposites. The experimental results indicated that a Co(II)@2-BPy@APTES@MHNTs/H₂O₂ catalytic system not only exhibits immense catalytic potential in accelerating the degradation process but also shows impressive features such as shorter reaction time and ambient reaction conditions. With the assistance of coumarin fluorescent probe technique and radical scavenging studies, the mechanistic pathway has been proposed, and it has been found that *in situ* generated highly reactive hydroxyl radicals play a crucial role in achieving outstanding degradation efficiency. The kinetic characteristics of the degradation profile demonstrate that pseudo-first-order kinetics is followed with an apparent rate constant of 0.1179 min⁻¹ for BPA and 0.1242 min⁻¹ for MG. Fascinatingly, the splendid magnetic properties of the designed Co(II)@2-BPy@APTES@MHNTs furnished their facile recovery and reusability for nine subsequent runs. Remarkably, the new findings demonstrated here will deepen our understanding of the fabrication and utilization of heterogeneous catalysts for wastewater treatment *via* a greener approach.

Received 3rd May 2022,
Accepted 7th July 2022

DOI: 10.1039/d2ma00500j

rsc.li/materials-advances

Introduction

Clean water and sanitation have been globally recognized as one of the sustainable development goals (SDGs) outlined by various member countries of U.N. in the year 2015 when the entire world arrived at a common consensus of accomplishing the goals within the time frame of fifteen years, *i.e.* by 2030.^{1,2} The global population has not only been increasing every year but also resulting in increased urbanization and anthropogenic activities, which have, in turn, jeopardized the quality of water severely due to increased disposal of detrimental compounds in water bodies.^{3,4} Synthetic dyes, pesticides, pharmaceuticals,

personal care products and organic pollutants are among the most common water pollutants that have exerted adverse effects on human survival and ecological environment even at low exposure levels. Bisphenol A (2,2-(4,4-dihydroxydiphenyl)propane, BPA) has been widely used as an important industrial precursor in the production of polyacrylates, polycarbonates, epoxy resins, polyester plastics, flame retardants and other chemical products such as baby bottles, food storage containers, toys, medicinal equipment, reusable drink containers, bar soaps, and shaving cream.^{5,6} Being highly soluble and stable in water, it gets easily leached from these materials and migrates into different aquatic streams, which ultimately results in the accumulation of BPA in the human body. Moreover, BPA has the tendency to mimic endogenous hormones, thereby causing sexual dysfunction, infertility, cancer (breast cancer, neuroblastoma), neurological disorders and cardiovascular diseases. Apart from this, synthetic water-soluble cationic dyes like malachite green

Green Chemistry Network Centre, Department of Chemistry, University of Delhi,
New Delhi-110007, India. E-mail: rksharmagreenchem@hotmail.com;
Fax: +91-011-27666250; Tel: +91-011-27666250

† Electronic supplementary information (ESI) available. See DOI: <https://doi.org/10.1039/d2ma00500j>



(MG) that are used extensively in papermaking, food, leather, textile and cosmetic industries are carcinogenic, teratogenic and mutagenic, thus posing a serious threat.^{7,8} The toxicity associated with the contaminants has created an alarming situation, which needs to be tackled immediately at a realistic scale. Till date, various methods such as adsorption, biological treatment, coagulation processes, solvent extraction, precipitation, membrane separation, electrochemical oxidation and ion-exchange have been employed for the treatment of polluted water.^{9–11} However, these strategies are limited by a series of factors including incomplete degradation of effluents, sludge generation, harsh reaction conditions, high cost and tedious workup process. As a promising alternative in water remediation techniques, Fenton or Fenton-like reactions, one of the most efficient advanced oxidation processes (AOPs), have recently gained immense popularity due to excellent potency in degrading organic contaminants into harmless products.¹² A plethora of methodologies are enlisted in the literature for the removal of BPA and MG, but these approaches encountered serious drawbacks such as lesser degradation efficiency, prolonged reaction time, harsh conditions and catalyst retrievability and reusability, which restrict their large-scale practical applicability.^{13–34} Therefore, a great array of endeavours need to be dedicated towards the fabrication and exploration of new catalytic materials, which not only overcome the above-mentioned challenges but also meet the criteria of green chemistry.^{35–37} In this regard, engineered halloysite nanotube-based nanocomposites have recently emerged at the forefront as excellent heterogeneous catalytic systems. Naturally occurring one-dimensional halloysite nanotubes (HNTs) belong to a class of hydrated layered aluminosilicates with a chemical composition of $\text{Al}_2\text{Si}_2\text{O}_5(\text{OH})_4 \cdot 2\text{H}_2\text{O}$ in a 1:1 proportion of Al:Si. The structure of HNTs consists of 15–20 rolled aluminosilicate layers, where the inner surface is composed of a gibbsite octahedral sheet of aluminol (Al–OH) groups, while the outer surface contains tetrahedral siloxane (Si–O–Si) groups.^{38,39} In recent years, HNTs have completely revolutionized the realm of materials science, due to the various fascinating properties such as hollow lumen structure, large surface area, high aspect ratio, great mechanical stability, high porosity, excellent thermal stability (up to 1200 °C), rich surface hydroxyl groups and tunable surface chemistry.⁴⁰ By taking privilege of the aforementioned features, HNTs serve as promising heterogeneous solid supports in diverse areas such as drug delivery, catalysis, sensing, absorption, photonics, fibre spinning, rubber fillers, enzyme immobilization, and ion-exchange.⁴¹ Regardless of a copious number of benefits, HNTs still suffer from the problem of facile retrievability and reusability. In order to circumvent these challenges, incorporating the magnetic responses of Fe_3O_4 nanoparticles to the surface of HNTs is worth applauding, which furnished quick recoverability through the assistance of external magnets.^{42–44} Furthermore, organo-silane functionalization has provided an unprecedented platform for the introduction of desired active groups on the surface of materials.

Enthused by the advantages offered by magnetic halloysite nanotubes (MHNTs) as potent heterogeneous catalytic supports

and in conjugation with our recent research interest in the design and development of hybrid organic–inorganic nanomaterials for wastewater treatment and various organic transformations,^{45–49} we herein describe the fabrication of magnetically retrievable halloysite-based cobalt nanocatalysts ($\text{Co(II)}@2\text{-BPy}@ \text{APTES}@ \text{MHNTs}$). To our delight, we found that the newly designed cobalt-based catalyst reveals splendid catalytic efficiency in the oxidative degradation of noxious bisphenol A (BPA) and malachite green (MG) under optimal reaction conditions. With the combination of various marvellous features such as shorter reaction time, high degradation efficiency, quick magnetic separation, excellent stability and durability, the present protocol has proven its superiority to all previously reported ones. To the best of our understanding, this work presents the first example of a newly fabricated magnetic halloysite-based cobalt nanocatalyst that manifests great prospects for enhanced degradation as well as offers a practically operational and environmentally benign route, which aroused interest among the scientific fraternity for treatment of organic pollutants in water.

Results and discussions

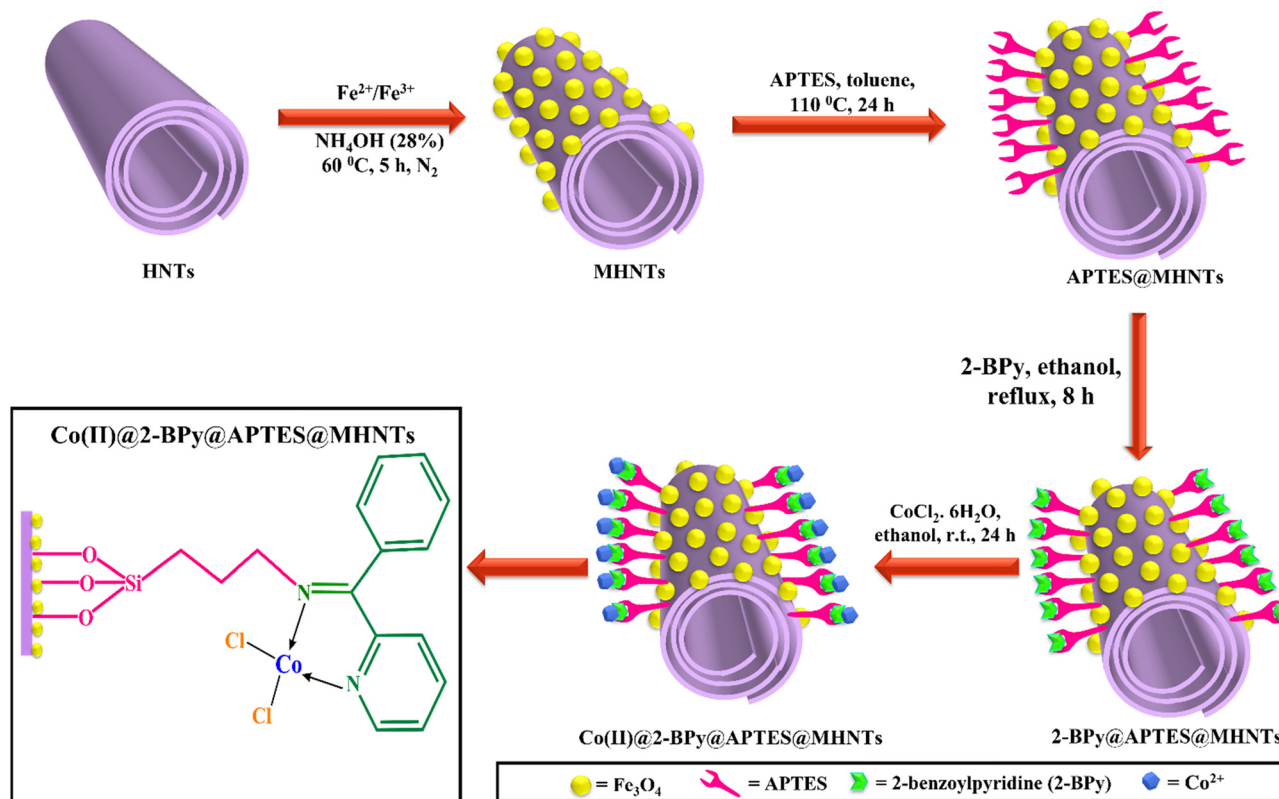
The catalyst preparation strategy fundamentally relies on the surface engineering of the magnetic halloysite nanotubes using a covalent grafting technique, which was conducted in a stepwise manner (Scheme 1). Initially, the halloysite nanotubes were decorated with ferrite nanoparticles by a co-precipitation technique.

Anchoring of Fe_3O_4 NPs appeared to be a beneficial step because ferrite imparts imperishable magnetism to the catalyst, which facilitates its magnetic retrievability from the reaction media. Thereafter, the resulting MHNTs were functionalized with 3-aminopropyltriethoxysilane (APTES) to render the material amenable for further modification (ligand grafting and subsequently metalation). Apparently, APTES works as a good functionalizing agent for incorporating amino groups onto the surface of various matrices. Further, the immobilization of the ligand (2-BPy) onto the surface of APTES@MHNTs and metalation using cobalt chloride were achieved successively, which have been described in-depth in the experimental section. Moreover, the synthesized $\text{Co(II)}@2\text{-BPy}@ \text{APTES}@ \text{MHNTs}$ nanocatalyst exhibits numerous unique characteristics such as enhanced degradation efficiency, incredible stability, ready recoverability, excellent recyclability and reusability. It is interesting to note that hydrogen peroxide (H_2O_2) acts as a fuel for generating active hydroxyl radical species, which further plays a crucial role towards expediting the degradation process. All the nanomaterials synthesized in steps were characterized thoroughly with the aid of advanced microscopic and spectroscopic techniques. Finally, the activity of the magnetic halloysite-supported cobalt catalyst was investigated in the degradation of BPA and MG.

Characterization of the designed catalyst

FT-IR spectroscopy. FT-IR analysis was performed to corroborate the stepwise grafting of various surface-modifying entities while synthesizing desired nanocatalysts. Fig. 1 represents





Scheme 1 Schematic description of the synthesis of a Co(II)@2-BPy@APTES@MHNTs nanocatalyst.

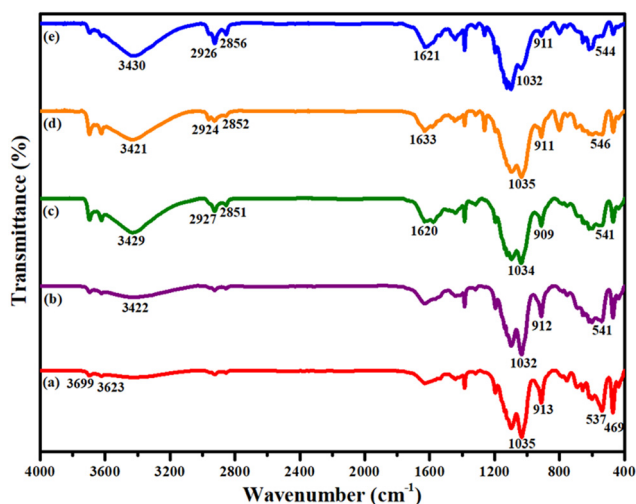


Fig. 1 FT-IR spectra of (a) HNTs, (b) MHNTs, (c) APTES@MHNTs, (d) 2-BPy@APTES@MHNTs and (e) Co(II)@2-BPy@APTES@MHNTs.

the FT-IR spectra of HNTs, MHNTs, APTES@MHNTs, 2-BPy@APTES@MHNTs and Co(II)@2-BPy@APTES@MHNTs. The spectrum of native HNTs clearly displays the characteristic peak of stretching mode of the inner layer hydroxyl group and inner-surface Al-OH groups are centred at 3699 cm^{-1} and 3623 cm^{-1} respectively. The appearance of strong and intense peak at 1035 cm^{-1} is assignable to the stretching mode of the Si-O-Si

bond, whereas absorption peaks centred at 913 cm^{-1} , 537 cm^{-1} and 469 cm^{-1} are attributable to the characteristic deformation vibrations of inner layer hydroxyl groups, Al-O-Si and Si-O-Si groups respectively.^{50,51} Moreover, it can be seen from the FT-IR spectra of MHNTs that all the characteristic peaks of HNTs not only remain constant, but an intense peak that belongs to the stretching vibrations of -OH groups from iron oxide also emerges at 3422 cm^{-1} . Apart from this, the characteristic absorption peak that appears around 580 cm^{-1} for Fe-O stretching vibration is not clearly observed, which is attributed to the fact that the peak corresponds to the bending vibrations of Al-O-Si possibly overlapping with it.^{52,53} On moving to the spectra of APTES@MHNTs, new distinguishable peaks emerging at 3429 , 2927 , 2851 and 1620 cm^{-1} are accredited to the asymmetric stretching mode of the amino (-NH₂) group, asymmetric stretching vibration of the -CH₂ group, symmetric stretching of -CH₂ and bending vibration assessments of the -NH group, providing strong evidence for the successful grafting of APTES on the surface of MHNTs. Furthermore, an enhanced sharp peak emerging at 1633 cm^{-1} in the 2-BPy@APTES@MHNTs FT-IR spectrum belongs to the -C=N stretching vibrations that validate the covalent immobilization of 2-BPy onto the surface of APTES@MHNTs *via* Schiff base condensation. Indeed, it is appreciable to mention that even after metalation of 2-BPy@APTES@MHNTs, all the inherent peaks appear in the final nanocatalyst, suggesting that the basic backbone structure remains completely intact. Nevertheless, a



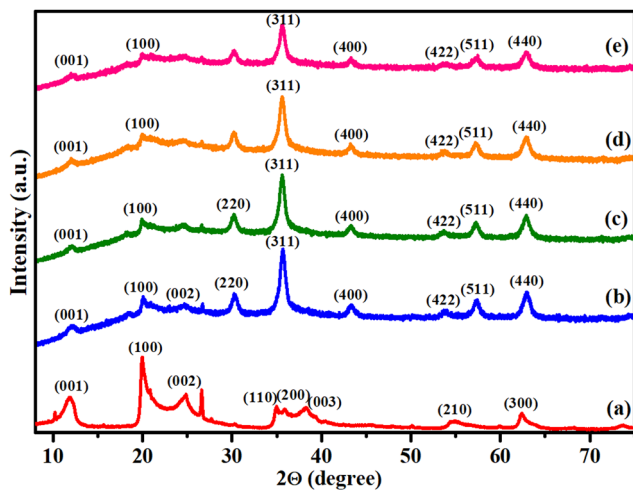


Fig. 2 P-XRD spectra of (a) HNTs, (b) MHNTs, (c) APTES@MHNTs, (d) 2-BPy@APTES@MHNTs and (e) Co(II)@2-BPy@APTES@MHNTs.

slight shift (*i.e.*, 1621 cm^{-1}) is observed in the value of absorption peak of $\text{C}=\text{N}$, which can be attributed to the coordinative linkage formation between the metal and the ligand.^{54,55}

P-XRD. To gain an insight into the structural integrity and crystalline phase structure of synthesized nanomaterials, the P-XRD technique was carried out under atmospheric conditions. The P-XRD spectrum of bare HNTs displayed in Fig. 2 exhibits characteristic peaks at specific $2\theta = 11.86^\circ, 19.98^\circ, 24.82^\circ, 35.02^\circ, 36.03^\circ, 38.30^\circ, 54.82^\circ,$ and 62.41° . These observed peaks are correspondingly attributed to the (001), (100), (002), (110), (200), (003), (210) and (300) crystal planes respectively, which are in good agreement with the Joint Committee on Powder Diffraction Standards data (JCPDS card no.: 29-1487).^{56,57} In the P-XRD spectrum of MHNTs, the appearance of six new strong diffraction Bragg's peaks at $2\theta = 30.18^\circ, 35.66^\circ, 43.37^\circ, 53.83^\circ, 57.34^\circ$ and 62.90° along with the HNTs peaks validates the decoration of the HNTs surface with Fe_3O_4 NPs. Moreover, the obtained characteristic peaks are accordingly assigned to the (220), (311), (400), (422), (511) and (440) crystal planes of cubic inverse spinel structure of Fe_3O_4 , corroborating the anchoring of iron oxide NPs onto the HNTs surface.⁵⁸ Furthermore, on moving to the P-XRD spectra of APTES@MHNTs and 2-BPy@APTES@MHNTs, similar diffraction peaks appeared at the same 2θ values along with a slight decrease in the intensity. However, no additional peaks were obtained in the P-XRD spectrum of Co(II)@2-BPy@APTES@MHNTs, implying the retention of crystalline nature and purity of samples even after the successive surface modifications.

VSM. VSM analysis was employed to deduce the magnetic attributes of synthesized nanocomposites MHNTs, APTES@MHNTs, 2-BPy@APTES@MHNTs and Co(II)@2-BPy@APTES@MHNTs with an applied magnetic field swept from $-10\,000$ Oe to $10\,000$ Oe under atmospheric conditions. From Fig. 3, it can be clearly observed that the flat curve passes through the origin, indicating the absence of magnetic characteristics in pristine HNTs. However, for other synthesized nanocomposites, an

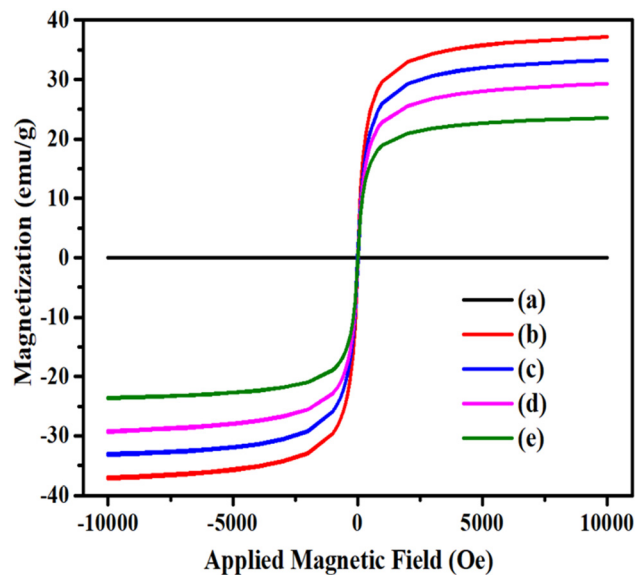


Fig. 3 Magnetization curves obtained via VSM for (a) HNTs, (b) MHNTs, (c) APTES@MHNTs, (d) 2-BPy@APTES@MHNTs and (e) Co(II)@2-BPy@APTES@MHNTs.

S-shaped curve appeared, which implies that these are superparamagnetic in nature.

Further, it was observed that the saturation magnetization value of MHNTs (36.91 emu g^{-1}) considerably decreased on moving to APTES@MHNTs (32.96 emu g^{-1}) and 2-BPy@APTES@MHNTs (29.14 emu g^{-1}). This gradual decrease in the M_s values could be ascribed to the grafting of surface-modifying entities onto bare MHNTs, which led to a reduction in surface moments of individual ferrite nanoparticles. Moreover, it is quite apparent from the VSM curves that the M_s value further dropped on moving from 2-BPy@APTES@MHNTs (29.14 emu g^{-1}) to the final nanocatalyst (23.65 emu g^{-1}), which was presumably due to the decoration of metal ions. Nevertheless, the net magnetism of the final nanocatalyst is found to be sufficiently good for its rapid and facile isolation from the reaction mixture with the aid of an external magnetic force.

Morphological studies. After determining the crystallinity and magnetic attributes, we shifted our focus towards investigating the structural and morphological changes that occurred during the synthesis of Co(II)@2-BPy@APTES@MHNTs. For this purpose, TEM and FE-SEM techniques were employed. From the TEM micrograph of bare HNTs displayed in Fig. 4, a hollow tubular cylindrical morphology was observed along with an open-ended lumen. The TEM image of MHNTs displayed a fine deposition of Fe_3O_4 NPs onto the outer surface of HNTs, affirming the successful fabrication of MHNTs. Moreover, the appearance of white spotty diffraction rings in the selected-area electron diffraction (SAED) pattern of MHNTs validate that Fe_3O_4 nanoparticles are polycrystalline in nature. These rings are correspondingly assigned to the [220], [311], [400], [422], [511], and [440] planes of the cubic inverse spinel structure of ferrite. Besides, through a closer introspection of



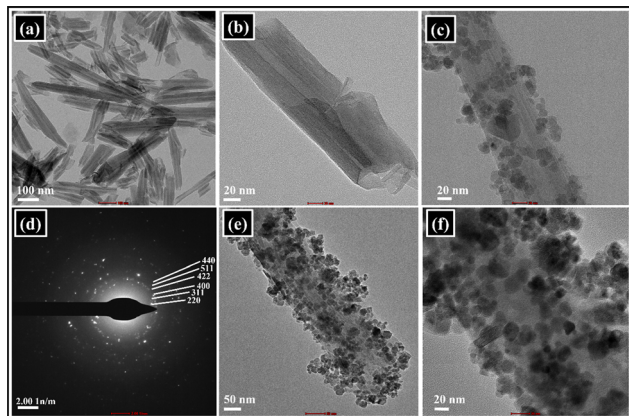


Fig. 4 TEM images of (a and b) HNTs (100 nm, 20 nm), (c) MHNTs, (d) SAED pattern of Fe_3O_4 and (e and f) $\text{Co(II)}@2\text{-BPy}@APTES@MHNTs$ (50 nm, 20 nm).

the TEM images of synthesized $\text{Co(II)}@2\text{-BPy}@APTES@MHNTs$, it was found that $\text{Co(II)}@2\text{-BPy}@APTES@MHNTs$ exhibited analogous morphology to the MHNTs, justifying the fact that the incorporation of various surface-modifying entities does not alter the crystalline morphological characteristics of MHNTs.

In addition, to shed light on the surface topographic attributes of HNTs, MHNTs and $\text{Co(II)}@2\text{-BPy}@APTES@MHNTs$, FE-SEM analysis was carried out. A thorough analysis of the FE-SEM micrograph of native HNTs (Fig. 5) revealed the tubular structure along with the smooth surface. Furthermore, from the FE-SEM image of MHNTs, it is quite evident that Fe_3O_4 particles with the spherical morphology have been appreciably decorated onto the surface of native HNTs.

Moreover, the FE-SEM images are in good agreement with the TEM images of $\text{Co(II)}@2\text{-BPy}@APTES@MHNTs$, authenticating that even after the grafting of discrete surface-modifying functionalities, the morphology remained intact.

XPS. The X-ray photoelectron spectra were recorded to gain a deeper insight into the surface chemical composition and binding states of different entities present in $\text{Co(II)}@2\text{-BPy}@APTES@MHNTs$. Fig. 6 displays the primary survey scan spectrum, which revealed the presence of Al (2p), Si (2p), C (1s), N (1s), O (1s), Fe (2p) and Co (2p). As displayed in the core level spectra of Al (2p) and Si (2p), peaks of Al–O and Si–O appear at 74.10 eV and 102.10 eV respectively (Fig. S1, ESI[†]).⁵⁹ According to the core level spectra of C 1s, peaks centred at 284.16 eV, 284.71 eV and 285.37 eV are ascribed to the C–C, C=C and C–N=C bonds. In addition, three characteristic peaks emerging

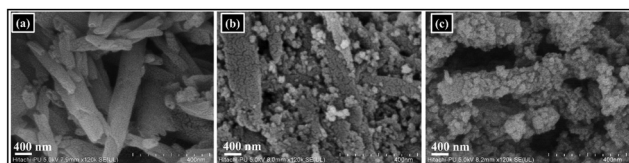


Fig. 5 FE-SEM images of (a) HNTs, (b) MHNTs and (c) $\text{Co(II)}@2\text{-BPy}@APTES@MHNTs$.

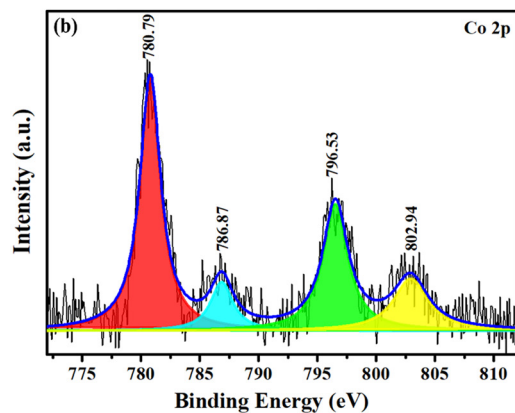
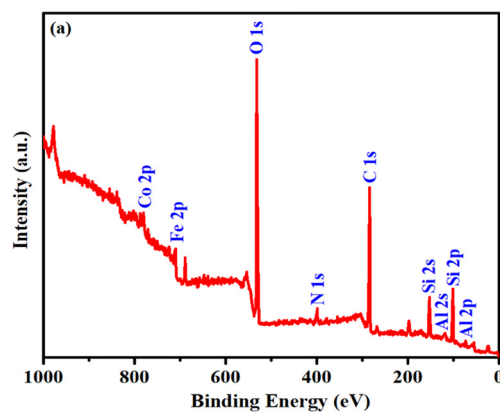


Fig. 6 Full range survey scan XPS spectrum of (a) $\text{Co(II)}@2\text{-BPy}@APTES@MHNTs$ and (b) core level region spectrum of Co 2p.

at 529.57 eV, 531.41 eV and 532.08 eV in the core level spectra of O 1s are accordingly assigned to Fe–O, Al–O and Si–O.

Moreover, on moving to the high-resolution XPS spectrum of N 1s, the peak positioned at 399.63 eV corresponds well with the C=N bond, affirming the successful immobilization of ligands *via* Schiff base condensation.⁶⁰ A detailed analysis of the high-resolution XPS spectrum of Fe 2p divulged two characteristic peaks at 709.63 eV (Fe 2p_{3/2}) and 723.34 eV (Fe 2p_{1/2}), which validated that iron is present in its +2 oxidation state. Moreover, the peaks at 711.35 (Fe 2p_{3/2}) and 724.57 eV (Fe 2p_{1/2}) are in good accordance with the trivalent state of iron, affirming the successful decoration of Fe_3O_4 NPs on the HNTs surface.^{61,62} Besides, the core level spectrum of Co 2p exhibits binding energy peaks at 780.79 eV and 786.87 eV, which match well with Co 2p_{3/2}, while the peaks at 796.53 eV and 802.94 eV are correspondingly attributed to Co 2p_{1/2}, which confirms the existence of +2 oxidation state of cobalt in $\text{Co(II)}@2\text{-BPy}@APTES@MHNTs$.^{63,64}

Compositional analysis. EDS and ED-XRF are the powerful tools that provide the information related to the elemental composition of discrete elements present in synthesized nanocomposites. Fig. 7 displays the ED-XRF, EDS and elemental mapping images of $\text{Co(II)}@2\text{-BPy}@APTES@MHNTs$. The emergence of a well-resolved peak of cobalt in the ED-XRF spectrum of $\text{Co(II)}@2\text{-BPy}@APTES@MHNTs$ corroborates the successful metalation of ligand-modified amine-functionalized magnetic halloysite nanotubes. As compared with the EDS spectrum of



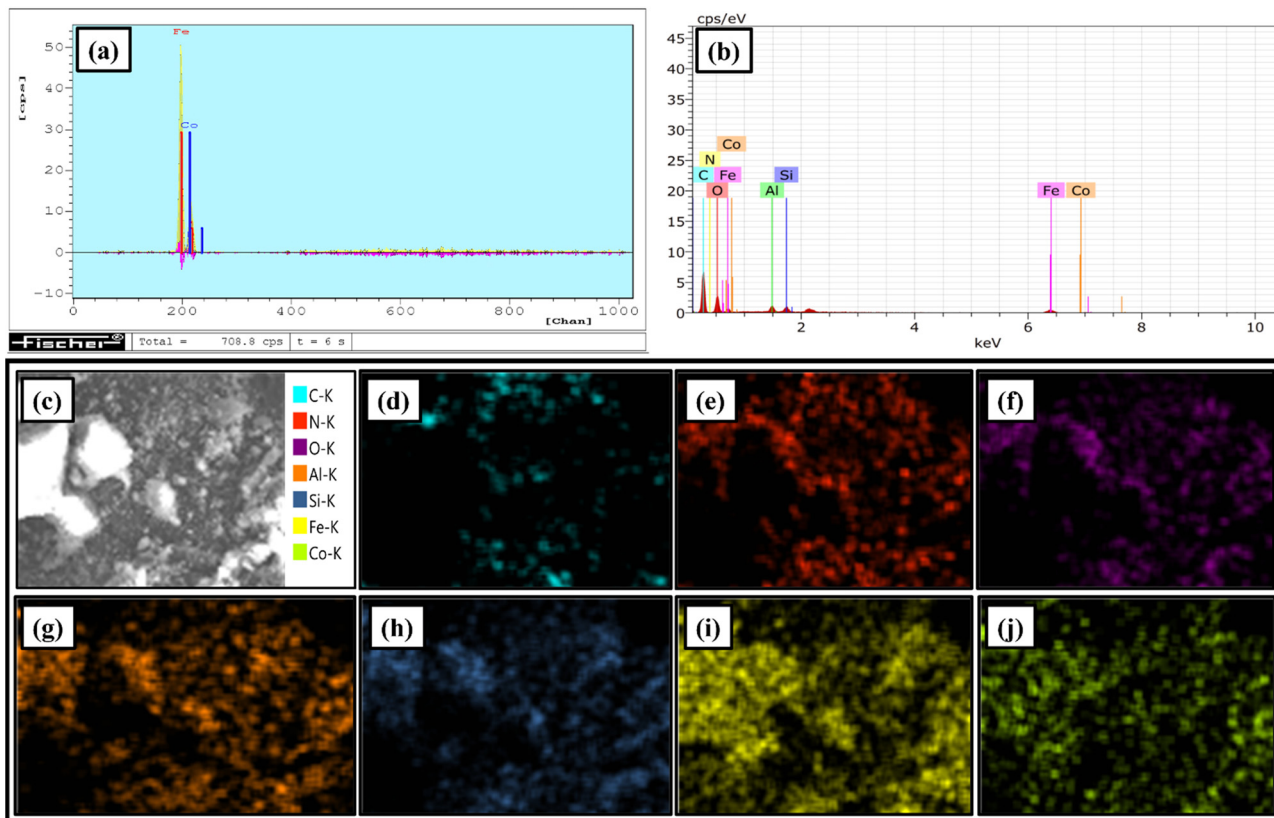


Fig. 7 (a) ED-XRF spectrum, (b) EDS spectrum of Co(II)@2-BPy@APTES@MHNTs, (c) SEM image of Co(II)@2-BPy@APTES@MHNTs and corresponding elemental mapping images of (d) carbon (e) nitrogen (f) oxygen (g) aluminium (h) silicon (i) iron and (j) cobalt.

bare HNTs (Fig. S2, ESI[†]), the Co(II)@2-BPy@APTES@MHNTs spectrum displayed well-defined peaks of Co, Fe, C and N along with Al, Si and O, validating the successful grafting of different surface-modifying entities. Moreover, the EDS elemental mapping images clearly reveal the presence of C, N, O, Al, Si, Fe and Co elements, authenticating the successful synthesis of Co(II)@2-BPy@APTES@MHNTs. Furthermore, the specific surface area and pore size distribution of Co(II)@2-BPy@APTES@MHNTs were determined by N₂ adsorption-desorption isotherms at 77 K (Fig. S3, ESI[†]). The specific surface area of nanocatalyst was measured to be 30.524 m² g⁻¹ using the Brunauer-Emmett-Teller (BET) equation. Besides, the pore size distribution was determined through density functional theory (DFT) curves, which displayed that the pore volume was 0.1943 cc g⁻¹ and the pore width was found to be 26.42 nm. Apart from this, the quantitative estimation of the amount of cobalt present in the designed Co(II)@2-BPy@APTES@MHNTs nanocomposite was evaluated by atomic absorption spectrometry (AAS) analysis and the corresponding content of cobalt was estimated to be 0.4073 mmol g⁻¹.

Evaluation of the catalytic activity of Co(II)@2-BPy@APTES@MHNTs in the degradation of BPA and MG. After successfully determining the structural and compositional attributes of the newly developed cobalt nanocatalyst, we further explored its catalytic efficiency in the degradation of BPA and MG. For the reaction to be governed under most

compatible conditions, the study of effect of various thermodynamic and kinetic parameters such as the amount of catalyst, amount of oxidant, pH and initial concentration of pollutants was carried out. With such objective in mind, a series of controlled experiments were performed, wherein the reaction was first conducted in the absence of the catalyst (Table 1).

The obtained results indicated that under such conditions, the reaction failed to occur, suggesting the need of a potent catalyst in driving the degradation process. Furthermore, other nanocomposites were also screened under similar reaction profiles, but found to be totally ineffective for catalysing the

Table 1 Determination of the catalytic potency of different catalysts on the degradation of BPA^a and MG^b

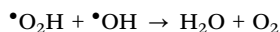
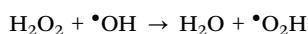
Sr. No	Catalyst	Degradation efficiency ^a (%)	Degradation efficiency ^b (%)
1	No catalyst	20.30	25.88
2	HNTs	21.76	26.63
3	MHNTs	30.26	34.73
4	APTES@MHNTs	26.53	32.16
5	2-BPy@APTES@MHNTs	23.19	28.14
6	Co(II)@2-BPy@APTES@MHNTs	96.93	97.89

^a Reaction conditions: 50 mL of BPA stock solution (68 mg L⁻¹), 0.5 mL of H₂O₂, 8 mg of catalyst, pH = 7, 30 min, r.t., λ_{max} = 276 nm. ^b Reaction conditions: 50 mL of MG stock solution (36 mg L⁻¹), 0.8 mL of H₂O₂, 10 mg of catalyst, pH = 7, 30 min, r.t., λ_{max} = 617 nm.



reaction. A thorough analysis of the results concluded that by using Co(II)@2-BPy@APTES@MHNTs, outstanding catalytic degradation efficiency could be achieved. Next, we also evaluated the significance of oxidants in conducting the concerned degradation of BPA (Fig. S4, ESI[†]) and MG (Fig. S5, ESI[†]). Considering this, the reaction was performed in the absence of oxidant (*i.e.*, only in the presence of catalyst). Almost negligible degradation efficiency of contaminants was observed, which led to the conclusion that presence of both the oxidant and catalyst is highly imperative in the reaction for attaining maximum degradation efficiency.

Amount of oxidant. Being a major factor in Fenton or Fenton-like oxidation, the study pertaining to the effect of hydrogen peroxide dosage on the overall degradation efficiency of pollutants is necessary. Therefore, to evaluate its effect on model reaction, we simply conducted a series of experiments, wherein the amount of oxidant was varied by maintaining the other parameters constant. It can be explicitly seen from Fig. 8 that under oxidant-free conditions, reactions did not proceed, while upon increasing the concentration of oxidant from 0.1 mL to 0.5 mL and 0.2 mL to 0.8 mL, the degradation efficiency of pollutants significantly increases from 35.92% to 96.93% and 33.25% to 97.89% for BPA and MG respectively. The obtained outcomes highlighted the fact that higher concentrations of oxidant led to the generation of a large number of highly reactive $\cdot\text{OH}$ radicals, which are responsible for driving the degradation process. In consideration of this, the oxidant dosage was further increased from 0.5 mL to 0.6 mL and 0.8 mL to 1.0 mL for BPA and MG respectively. Surprisingly, a decrease in the degradation efficiency was observed, which could be attributed to the scavenging effect of excessive H_2O_2 . More specifically, a greater amount of H_2O_2 escalated the inhibition of $\cdot\text{OH}$ radicals and subsequently resulted in the generation of least reactive $\cdot\text{O}_2\text{H}$ radicals, as described in the following equation:



Hence, a detailed inspection of the results concluded that 0.5 mL for BPA and 0.8 mL for MG was the optimal amount

of oxidant to be used, which helps in achieving a higher degradation extent of pollutants.

Amount of catalyst. Another key parameter that has a tremendous impact on the degradation process is the amount of catalyst utilized in the reaction mixture. The effect of catalyst loading was studied by increasing its amount in the reaction from 0 to 10 mg and 0 to 12 mg for respective BPA and MG. It was observed from the results displayed in Fig. 9 that the dose of catalyst in the reaction indeed affected the degradation process. Initially, we found that without Co(II)@2-BPy@APTES@MHNTs, no degradation of contaminants occurred under identical reaction conditions. However, an increase in the catalyst amount from 2 to 8 mg and 2 to 10 mg led to a drastic improvement in the degradation efficiency from 42.01% to 96.93% and 39.58% to 97.89% for BPA and MG respectively. This remarkable catalytic potency could be related to the presence of a greater surface area as well as a large number of accessible active sites delivered by the increased amount of catalyst in the reaction. Furthermore, when the catalyst dosage was further increased, a decrease in the extent of degradation of contaminants was observed during the reaction. The presence of excess amounts of catalyst would lead to its agglomeration in the reaction, as a result of which the available reactive sites and unit surface adsorption of H_2O_2 that accelerates the generation of $\cdot\text{OH}$ radicals get decreased. Conclusively, by using 8 mg and 10 mg amount of catalyst, BPA and MG pollutants could be degraded to their highest extent.

pH of the solution. The pH of the solution is another important parameter influencing the degradation of BPA and MG. Hence, to investigate the effect of pH on the degradation efficiency, the reaction was conducted by varying the pH from 3 to 11, while maintaining other parameters constant. The findings displayed in Fig. S6 (ESI[†]) clearly revealed that upon increasing the pH of the solution from 3 to 7, a significant increase in the degradation efficiency, *i.e.* from 48.64% to 97.89% for BPA and from 44.94% to 96.83% for MG was observed. This could be ascribed to the fact that under the acidic pH range, excess H^+ ions might react with H_2O_2 and transform H_2O_2 into more stable oxonium ions (H_3O_2^+). However, it was observed from the results that a further increase in solution pH from 7 to 11 caused a gradual decrease in the extent of

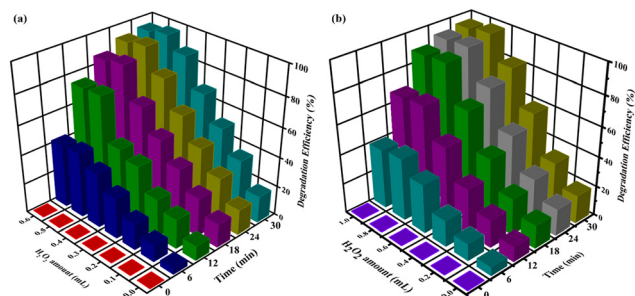


Fig. 8 Effect of H_2O_2 dosage on the catalytic degradation of (a) 50 mL of BPA stock solution (68 mg L^{-1}), x mL of H_2O_2 , 8 mg of catalyst, pH = 7, 30 min, r.t., $\lambda_{\text{max}} = 276 \text{ nm}$ and (b) 50 mL of MG stock solution (36 mg L^{-1}), y mL of H_2O_2 , 10 mg of catalyst, pH = 7, 30 min, r.t., $\lambda_{\text{max}} = 617 \text{ nm}$.

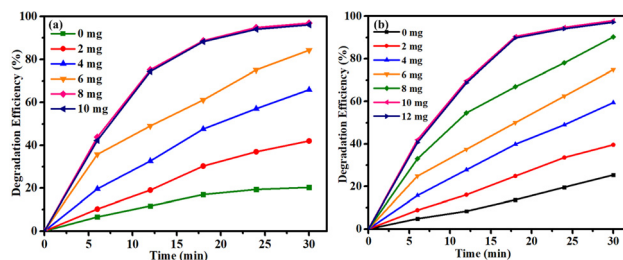


Fig. 9 Effect of the amount of catalyst on the catalytic degradation of (a) 50 mL of BPA stock solution (68 mg L^{-1}), 0.5 mL of H_2O_2 , x mg of catalyst, pH = 7, 30 min, r.t., $\lambda_{\text{max}} = 276 \text{ nm}$ and (b) 50 mL of MG stock solution (36 mg L^{-1}), 0.8 mL of H_2O_2 , y mg of catalyst, pH = 7, 30 min, r.t., $\lambda_{\text{max}} = 617 \text{ nm}$.



degradation under similar reaction conditions. The reason behind this could be attributed to the auto-decomposition of H_2O_2 to H_2O and O_2 at alkaline pH. Therefore, the above-mentioned results led to the conclusion that under a neutral pH (pH = 7), the degradation of BPA and MG was achieved to their maximum extent.

Amount of initial pollutants concentration. The initial concentration of pollutants plays a crucial role in achieving efficient degradation. Hence, in order to deduce the most favourable concentration of BPA and MG that could be treated efficiently, the model reaction was carried out in a diverse range of initial concentrations. The corresponding results are demonstrated in Fig. S7 (ESI[†]). Upon carefully analysing the results, it was found that the degradation rate was decreased drastically from 96.93% to 41.06% and 97.89% to 43.71% on increasing the initial concentration of BPA and MG from 68 mg L^{-1} to 98 mg L^{-1} and 36 mg L^{-1} to 90 mg L^{-1} respectively. As the initial concentration of BPA or MG was increased, the intermediates and a large number of contaminant molecules present in the reaction competed with each other to react with active $\cdot\text{OH}$ radicals. Evidently, with the adequate concentration of 68 mg L^{-1} and 36 mg L^{-1} of BPA and MG respectively, the $\text{Co(II)}@2\text{-BPy}@ \text{APTES}@ \text{MHNTs}$ nanocatalyst achieved the highest degradation efficiency.

Investigation of the catalytic activity of the nanocatalyst.

To shed light on the commendable catalytic efficiency possessed by newly fabricated $\text{Co(II)}@2\text{-BPy}@ \text{APTES}@ \text{MHNTs}$, oxidative degradation of water pollutants under optimal conditions was performed. The typical experiment was carried out in a round-bottomed flask in which a 50 mL of polluted water solution (BPA or MG) was taken. For this, an optimized amount of oxidant and catalyst both were added and stirred vigorously at room temperature for an appropriate reaction time. Afterwards, the reaction aliquots were withdrawn after every 3 min, and by using an external magnet, the catalyst was easily isolated from the solution. Furthermore, a UV-Vis spectrophotometer was used to measure the relative change in the absorbance initial values (A_0) of stock solutions and the separated sample solution within the range from 200 to 800 nm. During the reaction, the extent of degradation of pollutants using $\text{Co(II)}@2\text{-BPy}@ \text{APTES}@ \text{MHNTs}$ nanocatalyst can be easily determined using the following equation:

$$\text{Degradation efficiency } (D\%) = (A_0 - A_t)/A_0 \times 100$$

where D is designated as the degradation efficiency of pollutants, A_0 is the initial absorbance of the characteristic peak at $t = 0 \text{ min}$ and A_t is the absorbance at selected time intervals. The UV-Vis spectroscopy results indicated that BPA and MG exhibit maximum characteristic absorption peaks at 276 nm and 617 nm respectively. As the reaction time progressed, it can be seen that the absorption intensity of pollutants gradually decreased and finally got disappeared within a short time period of 30 min, indicating the complete removal of BPA and MG from water (Fig. S8, ESI[†]). With such phenomenal results, it is commendable to say that the combined effects of H_2O_2 and the $\text{Co(II)}@2\text{-BPy}@ \text{APTES}@ \text{MHNTs}$ achieved

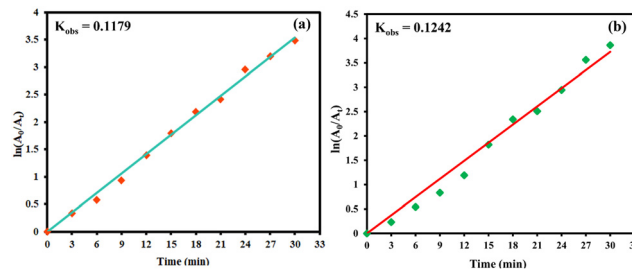


Fig. 10 Kinetic analysis for the oxidative degradation of (a) BPA and (b) MG.

splendid degradation efficiency and excellent TON (300.27 (BPA) and 106.98 (MG)) and TOF (600.54 h^{-1} (BPA) and 213.96 h^{-1} (MG)).

Kinetics. Having the optimized conditions in hand, the kinetics of catalytic oxidative degradation of BPA and MG could be systematically evaluated. To deduce the reaction kinetics, we simply plot a graph between $\ln(A_0/A_t)$ and reaction time (t), as displayed in Fig. 10. Based on these results, the BPA and MG degradation process seemed to follow pseudo-first-order kinetics, which is illustrated using the following equation:

$$\ln(A_0/A_t) = k_{\text{obs}}t$$

where t is the reaction time (min), A_0 and A_t corresponds to the initial absorbance and real-time absorbance at time $t = 0$ and $t = t$, respectively and k_{obs} is the apparent rate constant (min^{-1}). According to the above-mentioned study, k_{obs} was calculated as 0.1179 min^{-1} and 0.1242 min^{-1} for BPA and MG respectively.

Detection of $\cdot\text{OH}$ via fluorescence spectroscopy. During Fenton or Fenton-like oxidative reactions, hydroxyl radicals are considered as the prime active species that facilitate the degradation process. In order to validate this fact, we assessed a highly sensitive fluorescence probing technique wherein “coumarin”, a non-fluorescent probe moiety, was used. The typical process initiates when 10 mg of $\text{Co(II)}@2\text{-BPy}@ \text{APTES}@ \text{MHNTs}$ and 0.8 mL of H_2O_2 were added to the coumarin solution and allowed to stir vigorously under similar reaction conditions. Upon reacting with *in situ* generated hydroxyl radicals, coumarin produces a highly fluorescent adduct 7-hydroxycoumarin. Further, the fluorescence intensity of resulting supernatants was measured at an excitation wavelength of 334 nm, which resulted in the emergence of emission peak of 7-hydroxycoumarin at 456 nm (Fig. S9, ESI[†]). To our delight, we found that with the increase in the reaction time the emission intensity gradually increases, suggesting the formation of a large amount of hydroxyl radicals during the reaction. However, no significant fluorescent signal was observed when the reaction was carried out without adding the $\text{Co(II)}@2\text{-BPy}@ \text{APTES}@ \text{MHNTs}$ in the coumarin/ H_2O_2 system. From such interesting results, it is worth emphasizing that the $\text{Co(II)}@2\text{-BPy}@ \text{APTES}@ \text{MHNTs}/\text{H}_2\text{O}_2$ catalytic system drives the generation of reactive $\cdot\text{OH}$ that further actively participates in the degradation process. Moreover, to authenticate that *in situ* $\cdot\text{OH}$ is responsible for catalysing the oxidative degradation, we carried out a classical



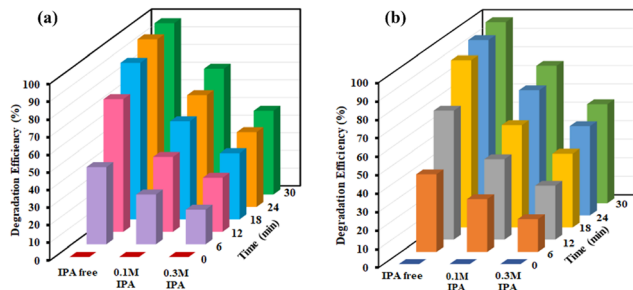


Fig. 11 The effects of the scavenger dosage on the degradation efficiency of (a) BPA (reaction conditions: 50 mL of stock solution (68 mg L^{-1}), 0.5 mL H_2O_2 , 8 mg catalyst, pH = 7, 30 min, r.t., $\lambda_{\text{max}} = 276 \text{ nm}$) and (b) MG (reaction conditions: 50 mL of stock solution (36 mg L^{-1}), 0.8 mL H_2O_2 , 10 mg catalyst, pH = 7, 30 min, r.t., $\lambda_{\text{max}} = 617 \text{ nm}$).

radical scavenging test. For this purpose, an efficient hydroxyl radical quencher isopropyl alcohol (IPA) was used in the reaction. As anticipated in Fig. 11 without adding IPA, the degradation efficiencies of respective BPA and MG were found to be 96.93% and 97.89% in 30 min. However, in the presence of 0.1 M of IPA, a tremendous decrease in the extent of degradation was observed, *i.e.* 71.26% for BPA and 74.37% for MG. Further, it was observed that the degradation rate reduced drastically with the increase in the concentration of quenching agent to 0.3 M. The obtained results are in good agreement with the fluorescence probing technique, indicating that $\cdot\text{OH}$ is the main active species that plays a remarkable role in catalysing the degradation reaction.

Mechanism. On the grounds of radical scavenging studies and previously reported protocols, a plausible mechanism was proposed for the degradation of pollutants, as displayed in Scheme S1 (ESI \dagger). During the reaction, *in situ* $\cdot\text{OH}$ radicals are formed by the interaction of catalyst and hydrogen peroxide. Initially, H_2O_2 molecules are adsorbed onto the surface of the catalyst, and they oxidize Co(II) to Co(III) along with generating reactive hydroxyl radicals.^{65–67} In the next step, the generated Co(III) reacts with another molecule of H_2O_2 , forming $\cdot\text{O}_2\text{H}$ radicals and regenerating Co(II) .⁶⁸ Following the two pathways, the $\cdot\text{O}_2\text{H}$ utilized in the reaction (i) either reacts itself and produce H_2O_2 (ii) or combines with H_2O_2 to form $\cdot\text{OH}$ radicals, facilitating the overall degradation process. Further, these $\cdot\text{OH}$ radicals attack pollutants and fragment them into smaller innocuous molecules such as CO_2 and H_2O .^{69,70}

Heterogeneity. In a quest to explore the intrinsic stability and heterogeneity of the newly fabricated $\text{Co(II)}@2\text{-BPy}@ \text{APTES}@ \text{MHNTs}$, a standard hot filtration test was carried out for the concerned reaction. For this, we performed the degradation of MG under optimal reaction conditions. After conducting the reaction for about 15 min (*i.e.* half of the actual time), the $\text{Co(II)}@2\text{-BPy}@ \text{APTES}@ \text{MHNTs}$ were facilely isolated from the solution using an external magnet. Even on keeping the remaining supernatant solution under stirring for prolonged duration (additional 15 min), no further increment in degradation efficiency was observed (Fig. 12). Hence, the obtained results corroborated the heterogenous character of the nanocatalyst, as no discernible leaching of cobalt from $\text{Co(II)}@2\text{-BPy}@ \text{APTES}@ \text{MHNTs}$ took place during the process.

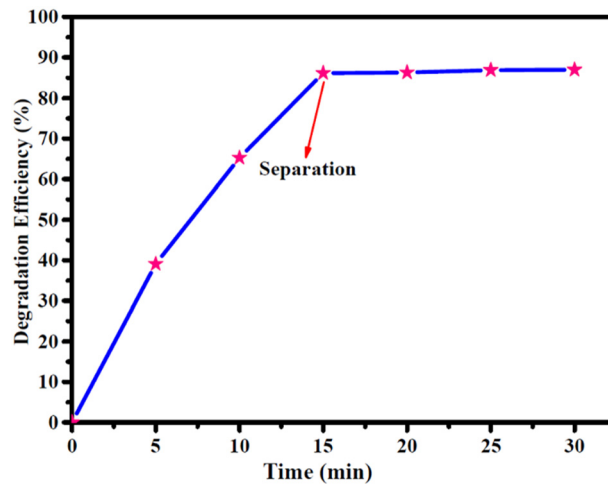


Fig. 12 Hot filtration experiment to evaluate the stability of $\text{Co(II)}@2\text{-BPy}@ \text{APTES}@ \text{MHNTs}$.

Reusability. After investigating the heterogeneity of $\text{Co(II)}@2\text{-BPy}@ \text{APTES}@ \text{MHNTs}$, other important parameters that need to be evaluated from commercial and industrial perspectives are retrievability and reusability. For scrutinizing the recyclability of the designed nanohybrid, a typical experiment was conducted under optimal reaction conditions, wherein repeated runs for degradation of MG were carried out in the presence of $\text{Co(II)}@2\text{-BPy}@ \text{APTES}@ \text{MHNTs}$. Upon completion of the degradation process, the catalyst was easily separated from the reaction mixture with the aid of an external magnet. Thereafter, the retrieved catalyst was washed thoroughly with water and ethanol in order to remove previous reaction residues and dried in an oven at $60 \text{ }^\circ\text{C}$. Furthermore, the dried catalyst was then subjected to successive runs of the same degradation process. From the results, it was concluded that the recovered $\text{Co(II)}@2\text{-BPy}@ \text{APTES}@ \text{MHNTs}$ not only displayed outstanding catalytic efficiency but could also be reused for nine consecutive cycles (Fig. 13). Interestingly, the obtained results were further supported by XRD, VSM, TEM and FE-SEM analyses (Fig. S10, ESI \dagger) of the retrieved $\text{Co(II)}@2\text{-BPy}@ \text{APTES}@ \text{MHNTs}$, indicating

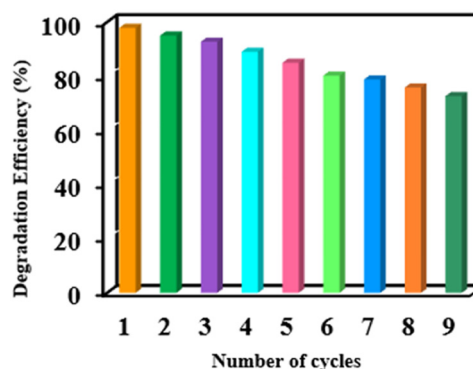


Fig. 13 Recyclability experiments involving $\text{Co(II)}@2\text{-BPy}@ \text{APTES}@ \text{MHNTs}$ and MG (reaction conditions: 50 mL of stock solution (36 mg L^{-1}), 0.8 mL of H_2O_2 , 10 mg catalyst, pH = 7, 30 min, r.t., $\lambda_{\text{max}} = 617 \text{ nm}$).



that crystallinity, magnetic behaviour as well as the morphology remained intact even after multiple catalytic runs.

Comparison of the catalytic efficiency of Co(II)@2-BPy@APTES@MHNTs with protocols reported in the literature.

A preliminary and brief literature survey has been carried out for establishing the superiority of the present protocol over the previously reported methodologies (Table S1, ESI[†]). Careful and deep analysis of results divulged that the designed Co(II)@2-BPy@APTES@MHNTs/H₂O₂ catalytic system exhibited a higher degradation efficiency in shorter time duration than the various existing catalysts. Moreover, lesser catalytic amounts of Co(II)@2-BPy@APTES@MHNTs are found to be highly effective for degrading BPA (Table S1, entries 5 and 8, ESI[†]) and MG (Table S1, entries 3 and 6, ESI[†]). Furthermore, in comparison to some of the previously reported methods, the present catalytic system does not require acidic conditions to degrade hazardous contaminants (BPA (Table S1 entries 2, 3 and 10, ESI[†]) and MG (Table S1 entries 1, 7 and 10, ESI[†])). Besides, it can be clearly seen that some of the previous methods displayed lesser degradation efficiency even if the reaction was carried out for prolonged time (BPA (Table S1, entries 1, 9 and 12, ESI[†]) and MG (Table S1, entries 5 and 9, ESI[†])). Hence, it is worth appreciating that the present catalytic system displayed its supremacy over previous protocols in terms of commendable degradation efficiency, ambient reaction conditions along with shorter reaction times and marvellous catalytic potency. In addition, the superparamagnetic behaviour of the catalyst offered rapid separation from the solution media, as a result of which the developed catalyst could be reused up to nine consecutive cycles.

Conclusion

In conclusion, we have successfully demonstrated a facile and stepwise approach for fabricating magnetically separable Co(II)@2-BPy@APTES@MHNTs heterogenous nanocomposites, which involves covalent immobilization of 2-BPy onto the surface of amino-silane-functionalised magnetic halloysite nanotubes followed by metalation. Various physico-chemical techniques such as P-XRD, TEM, FE-SEM, XPS, EDX, ED-XRF and FT-IR spectroscopy provided a deep insight into the morphology, magnetization and crystallinity of the newly synthesized nanocomposites. Further, the catalytic activity of Co(II)@2-BPy@APTES@MHNTs was investigated for the first time in the oxidative degradation of BPA and MG, which were used as model water contaminants. Moreover, to achieve the maximum degradation efficiency of pollutants, different reaction parameters such as the amount of catalyst, oxidant dosage, pH and initial pollutant concentration were studied. During the process, the designed Co(II)@2-BPy@APTES@MHNTs exhibit a superior degradation efficiency of 97.89% (BPA) and 96.83% (MG) within 30 min. Besides, the presence of the magnetically responsive attribute of the heterogeneous Co(II)@2-BPy@APTES@MHNTs nanocatalyst offers effortless magnetic retrievability. Moreover, a shorter reaction time, exceptional degradation efficiency, high

TON and TOF, absence of harsh chemicals, excellent recycling potential (up to nine consecutive runs), and ambient reaction conditions are some of the other interesting features that made the overall protocol highly sustainable and a better alternative to all other previously reported methodologies. Thus, we believe that the present work sheds light on the enormous potential of the designed nanocomposite, making it a promising candidate for eliminating recalcitrant water contaminants, as well as opens up new and promising possibilities for its usage in real-world applications.

Experimental

Synthesis of MHNTs

The synthetic approach for the fabrication of a magnetically retrievable nanocatalytic support (MHNTs) was based on the well-known co-precipitation technique.⁷¹ Initially, the synthetic protocol involved the addition of 0.5 g of native HNTs to 400 mL of distilled water, which was further ultrasonicated for 15 min. After the uniform dispersion of HNTs, 1.165 g of FeCl₃·6H₂O and 0.5 g of FeCl₂·4H₂O were added and stirred vigorously at 60 °C in nitrogen atmosphere. With progress in time, the colour of the solution turned to yellowish orange. Subsequently, 28% of NH₄OH solution was added dropwise to the above-mentioned reaction mixture till the pH of solution turned basic. The black precipitate of MHNTs was formed immediately as the base was added to the different salts of iron (Fe²⁺/Fe³⁺). The resulting solution was kept under stirring for further 5 h. Thereafter, the synthesized product was separated using an external magnet and successive washing was conducted with distilled water and ethanol until the pH of solution became neutral. Ultimately, the washed MHNTs were kept in an oven at 60 °C for drying.

Synthesis of APTES@MHNTs

For introducing the silane-functionalizing agent (APTES) onto the surface of MHNTs, 1.5 g of MHNTs was added into a round-bottomed flask containing 50 mL of dried toluene and homogeneously dispersed *via* ultrasonic irradiation for 20 min.⁷² The flask was fitted with a rubber septum and a condenser, and the reaction mixture was vigorously stirred in a nitrogen atmosphere. Afterwards, 5 mL of APTES solution was injected in a dropwise manner into the above-mentioned solution, which was then placed in an oil bath at a temperature of 110 °C and refluxed for 24 h at the same temperature. Once the reaction was completed, it was cooled down to the ambient temperature and the solid product was separated *via* an external magnetic force. Finally, it was washed thoroughly with ethanol to remove the unreacted aminosilane residues and dried under vacuum at 80 °C.

Synthesis of Co(II)@2-BPy@APTES@MHNTs

The synthesis of the Co(II)@2-BPy@APTES@MHNTs nanocatalyst was accomplished *via* a facile two-step procedure. At the outset, the fabrication of ligand-immobilized amine-functionalized



MHNTs was carried out, which involved the uniform dispersion of 1.5 g of APTES@MHNTs into 25 mL of ethanol. Thereafter, to the above-mentioned reaction suspension, 2-BPy was added and kept under continuous refluxing for 8 h to afford the desired 2-BPy@APTES@MHNTs nanocomposite.⁷³ After the reaction cooled down to room temperature, the resulting product was magnetically isolated, washed repeatedly and dried overnight in a vacuum drying chamber at 60 °C. In the subsequent step, an ethanolic solution of cobalt chloride was prepared to which 1.0 g of uniformly dispersed 2-BPy@APTES@MHNTs was added. Under vigorous stirring, the reaction was conducted at room temperature for 24 h. With the aid of an external magnet, the desired Co(II)@2-BPy@APTES@MHNTs were separated, extensively washed with ethanol and kept overnight in a vacuum chamber for drying.⁷⁴

General procedure for the reaction

To a 50 mL stock solution of BPA or MG taken in a round-bottomed flask, a certain amount of H₂O₂ was added. For the reaction to occur in a continuous manner, it was kept under vigorous stirring, and in the meantime, an appropriate amount of catalyst was added into the solution media. During this catalytic procedure, the reaction solution was withdrawn at predetermined time intervals using a syringe, and the catalyst was immediately retrieved using an external magnet. Further, using a UV-Vis spectrophotometer, changes in the absorbance intensity of the remaining supernatant solution were recorded during the reaction.

Conflicts of interest

There are no conflicts to declare.

Acknowledgements

Bhavya Arora, Sneha Yadav, Pooja Rana and Priyanka greatly acknowledge Council of Scientific and Industrial Research (CSIR) and University Grants Commission (UGC), Delhi, India for awarding research fellowships. Also, the authors thank to USIC, University of Delhi, India for FT-IR, VSM, XRD assistance, Punjab University for FE-SEM studies, AIIMS for TEM analysis and IIT Roorkee for XPS analysis. We are also thankful to Faculty Research Programme Grant – IoE and Department of Science and Technology (DST) (Grant ID: DST/TMDEWO/WTI2K19/EWFH/2019/290(G)) for awarding project for carrying work related to water remediation.

References

- X. Zhou, Z. Li, T. Zheng, Y. Yan, P. Li, E. A. Odey, H. P. Mang and S. M. N. Uddin, *Environ. Int.*, 2018, **120**, 246–261.
- V. Soltaninejad, M. R. Ahghari, R. Taheri-Ledari and A. Maleki, *Langmuir*, 2021, **37**, 4700–4713.
- J. Rahimi, R. Taheri-Ledari, M. Niksefat and A. Maleki, *Catal. Commun.*, 2020, **134**, 105850.
- R. Taheri-Ledari, K. Valadi, S. Gharibi and A. Maleki, *Mater. Res. Bull.*, 2020, **130**, 110946.
- D. Chen, F. Xiong, H. Zhang, C. Ma, L. Cao and J. Yang, *ACS Omega*, 2020, **5**, 1198–1205.
- X. Liang, G. Wang, X. Dong, G. Wang, H. Ma and X. Zhang, *ACS Appl. Nano Mater.*, 2018, **2**, 517–524.
- M. A. Salam, M. R. Abukhadra and A. Adlii, *ACS Omega*, 2020, **5**, 2766.
- D. C. Ghosh, P. K. Sen and B. Pal, *J. Phys. Chem. B*, 2020, **124**, 2048–2059.
- V. Soltaninejad and A. Maleki, *J. Photochem. Photobiol., A*, 2021, **404**, 112906.
- A. Maleki, M. Mohammad, Z. Emdadi, N. Asim, M. Azizi and J. Safaei, *Arab. J. Chem.*, 2020, **13**, 3017–3025.
- A. Maleki, Z. Hajizadeh, V. Sharifi and Z. Emdadi, *J. Cleaner Prod.*, 2019, **215**, 1233–1245.
- W. Ma, K. Wang, S. Pan and H. Wang, *Langmuir*, 2019, **36**, 6924–6929.
- C. M. Park, J. Heo and Y. Yoon, *Chemosphere*, 2017, **168**, 617–622.
- X. Yang, P. F. Tian, C. Zhang, Y. Q. Deng, J. Xu, J. Gong and Y. F. Han, *Appl. Catal., B*, 2013, **134**, 145–152.
- V. Cleveland, J. P. Bingham and E. Kan, *Sep. Purif. Technol.*, 2014, **133**, 388–395.
- S. A. Mirzaee, N. Jaafarzadeh, H. T. Gomes, S. Jorfi and M. Ahmadi, *Chem. Eng. J.*, 2019, **370**, 372–386.
- T. Bao, M. M. Damtie, A. Hosseinzadeh, W. Wei, J. Jin, H. N. P. Vo, J. S. Ye, Y. Liu, X. F. Wang, Z. M. Yu, Z. J. Chen and B. J. Ni, *J. Environ. Manage.*, 2020, **260**, 110105.
- L. Ma, H. He, R. Zhu, J. Zhu, I. D. Mackinnon and Y. Xi, *Catal. Sci. Technol.*, 2016, **6**, 6066–6075.
- B. Guo, T. Xu, L. Zhang and S. Li, *J. Environ. Manage.*, 2020, **272**, 111047.
- M. P. Pachamuthu, S. Karthikeyan, R. Maheswari, A. F. Lee and A. Ramanathan, *Appl. Surf. Sci.*, 2017, **393**, 67–73.
- K. Pan, C. Yang, J. Hu, W. Yang, B. Liu, J. Yang, S. Liang, K. Xiao and H. Hou, *J. Hazard. Mater.*, 2020, **389**, 122072.
- X. Zhang, Y. Ding, H. Tang, X. Han, L. Zhu and N. Wang, *Chem. Eng. J.*, 2014, **236**, 251–262.
- L. Zhang, D. Xu, C. Hu and Y. Shi, *Appl. Catal., B*, 2017, **207**, 9–16.
- M. Ahmadi, H. Rahmani, A. Takdastan, N. Jaafarzadeh and A. Mostoufi, *Process Saf. Environ. Prot.*, 2016, **104**, 413–421.
- M. Ergüt, D. Uzunoğlu and A. Özer, *J. Environ. Sci. Health A*, 2019, **54**, 786–800.
- Y. Hu, Y. Li, J. He, T. Liu, K. Zhang, X. Huang, L. Kong and J. Liu, *J. Environ. Manage.*, 2018, **226**, 256–263.
- F. V. De Andrade, A. B. De Oliveira, G. O. Siqueira, M. M. Lage, M. R. de Freitas, G. M. de Lima and J. Nuncira, *J. Environ. Chem. Eng.*, 2021, **9**, 106232.
- M. Hajnajafi, A. Khorshidi, A. G. Gilani and B. Heidari, *Res. Chem. Intermed.*, 2018, **44**, 3313–3323.
- E. Yabalak and F. Elneccar, *Biomass Convers. Biorefin.*, 2021, 1–13.
- D. B. Jiang, Y. Yuan, D. Zhao, K. Tao, X. Xu and Y. X. Zhang, *J. Nanoparticle Res.*, 2018, **20**, 1–10.



- 31 K. Dutta, S. Bhattacharjee, B. Chaudhuri and S. Mukhopadhyay, *J. Environ. Sci. Health A*, 2003, **38**, 1311–1326.
- 32 S. Saha and A. Pal, *Sep. Purif. Technol.*, 2014, **134**, 26–36.
- 33 Y. Wu, S. Zeng, F. Wang, M. Megharaj, R. Naidu and Z. Chen, *Sep. Purif. Technol.*, 2015, **154**, 161–167.
- 34 Z. Li, Z. Chen, Q. Zhu, J. Song, S. Li and X. Liu, *J. Hazard. Mater.*, 2020, **399**, 123088.
- 35 A. Maleki, Z. Varzi and F. Hassanzadeh-Afruzi, *Polyhedron*, 2019, **171**, 193–202.
- 36 Z. Varzi and A. Maleki, *Appl. Organomet. Chem.*, 2019, **33**, e5008.
- 37 A. Maleki, *Ultrason. Sonochem.*, 2018, **40**, 460–464.
- 38 H. Hamza, A. M. Ferretti, C. Innocenti, K. Fidecka, E. Licandro, C. Sangregorio and D. Maggioni, *Inorg. Chem.*, 2020, **59**, 12086–12096.
- 39 M. Rouhi, M. Babamoradi, Z. Hajizadeh, A. Maleki and S. T. Maleki, *Optik*, 2020, **212**, 164721.
- 40 C. E. Tas, E. B. Sevinis Ozbulut, O. F. Ceven, B. A. Tas, S. Unal and H. Unal, *ACS Omega*, 2020, **5**, 17962–17972.
- 41 H. Zhang, T. Ren, Y. Ji, L. Han, Y. Wu, H. Song, L. Bai and X. Ba, *ACS Appl. Mater. Interfaces*, 2015, **7**, 23805–23811.
- 42 A. Maleki, *RSC Adv.*, 2014, **4**, 64169–64173.
- 43 A. Maleki, *Tetrahedron Lett.*, 2013, **54**, 2055–2059.
- 44 A. Maleki, *Tetrahedron*, 2012, **68**, 7827–7833.
- 45 R. K. Sharma, B. Arora, S. Sharma, S. Dutta, A. Sharma, S. Yadav and K. Solanki, *Mater. Chem. Front.*, 2020, **4**, 605–620.
- 46 B. Arora, S. Sharma, S. Dutta, A. Sharma, S. Yadav, P. Rana, P. Rana and R. K. Sharma, *New J. Chem.*, 2022, **46**, 5405–5418.
- 47 S. Yadav, R. Dixit, S. Sharma, S. Dutta, B. Arora, P. Rana, B. Kaushik, P. Rana, A. Adholeya, M. B. Gawande and R. K. Sharma, *Mater. Chem. Front.*, 2021, **5**, 7343–7355.
- 48 S. Yadav, R. Dixit, S. Sharma, S. Dutta, B. Arora, P. Rana, B. Kaushik, K. Solanki and R. K. Sharma, *New J. Chem.*, 2022, **46**, 10829–10843.
- 49 S. Yadav, S. Sharma, S. Dutta, A. Sharma, A. Adholeya and R. K. Sharma, *Inorg. Chem.*, 2020, **59**, 8334–8344.
- 50 X. Wan, Y. Zhan, G. Zeng and Y. He, *Appl. Surf. Sci.*, 2017, **393**, 1–10.
- 51 Y. Zhang, X. He, J. Ouyang and H. Yang, *Sci. Rep.*, 2013, **3**, 1–6.
- 52 A. Maleki, Z. Hajizadeh and R. Firouzi-Haji, *Microporous Mesoporous Mater.*, 2018, **259**, 46–53.
- 53 Y. Xie, D. Qian, D. Wu and X. Ma, *Chem. Eng. J.*, 2011, **168**, 959–963.
- 54 G. R. Reddy and S. Balasubramanian, *RSC Adv.*, 2015, **5**, 53979–53987.
- 55 H. Ebrahimiasl and D. Azarifar, *Appl. Organomet. Chem.*, 2020, **34**, e5359.
- 56 A. B. Ganganboina, A. Dutta Chowdhury and R. A. Doong, *ACS Sustainable Chem. Eng.*, 2017, **5**, 4930–4940.
- 57 T. Zhu, C. Qian, W. Zheng, R. Bei, S. Liu, Z. Chi, X. Chen, Y. Zhang and J. Xu, *RSC Adv.*, 2018, **8**, 10522–10531.
- 58 J. Pan, H. Yao, L. Xu, H. Ou, P. Huo, X. Li and Y. Yan, *J. Phys. Chem. C*, 2011, **115**, 5440–5449.
- 59 S. C. Jee, M. Kim, S. K. Shinde, G. S. Ghodake, J. S. Sung and A. A. Kadam, *Appl. Surf. Sci.*, 2020, **509**, 145358.
- 60 A. Saroja and B. R. Bhat, *Ind. Eng. Chem. Res.*, 2018, **58**, 590–601.
- 61 X. Song, L. Zhou, Y. Zhang, P. Chen and Z. Yang, *J. Cleaner Prod.*, 2019, **224**, 573–582.
- 62 R. Nagarajan, P. Gupta, P. Singh and P. Chakraborty, *Dalton Trans.*, 2016, **45**, 17508–17520.
- 63 C. Ren, H. Li, R. Li, S. Xu, D. Wei, W. Kang, L. Wang, L. Jia, B. Yang and J. Liu, *RSC Adv.*, 2016, **6**, 33302–33307.
- 64 J. Sun, G. Yu, L. Liu, Z. Li, Q. Kan, Q. Huo and J. Guan, *Catal. Sci. Technol.*, 2014, **4**, 1246–1252.
- 65 F. Chen, X. Wu, R. Bu and F. Yang, *RSC Adv.*, 2017, **7**, 41945–41954.
- 66 Y. Shen, Z. H. Zhang and K. J. Xiao, *RSC Adv.*, 2015, **5**, 91846–91854.
- 67 A. M. I. Jayaseeli, A. Ramdass and S. Rajagopal, *Polyhedron*, 2015, **100**, 59–66.
- 68 E. Spier, U. Neuenschwander and I. Hermans, *Angew. Chem., Int. Ed.*, 2013, **52**, 1581–1585.
- 69 D. D. Dionysiou, M. T. Suidan, I. Baudin and J. M. Lainé, *Appl. Catal., B*, 2004, **50**, 259–269.
- 70 X. Guo, K. Wang and Y. Xu, *Mater. Sci. Eng., B*, 2019, **245**, 75–84.
- 71 A. A. Kadam, J. Jang and D. S. Lee, *ACS Appl. Mater. Interfaces*, 2017, **9**, 15492–15501.
- 72 A. B. Ganganboina, A. D. Chowdhury and R. A. Doong, *Electrochim. Acta*, 2017, **245**, 912–923.
- 73 T. Baran, İ. Sargın, M. Kaya, P. Mulerčikas, S. Kazlauskaitė and A. Menteş, *Chem. Eng. J.*, 2018, **331**, 102–113.
- 74 P. Chakraborty, S. Purkait, S. Mondal, A. Bauzá, A. Frontera, C. Massera and D. Das, *CrystEngComm*, 2015, **17**, 4680–4690.

